I&EC research
Industrial & Engineering Chemistry Research

Article

pubs.acs.org/IECR

Modification of Crystal Shape through Deep Temperature Cycling

Mo Jiang,[†] Xiaoxiang Zhu,[†] Mark C. Molaro,[†] Michael L. Rasche,[‡] Haitao Zhang,[†] Keith Chadwick,[§] Davide M. Raimondo,[▽] Kwang-Ki K. Kim,[†,‡] Lifang Zhou,[†] Zhilong Zhu,[‡] Min Hao Wong,[‡] Des O'Grady,[⊥] Dominique Hebrault,[⊥] John Tedesco,[⊥] and Richard D. Braatz*[,†,‡]

[†]Massachusetts Institute of Technology, 77 Massachusetts Avenue, Cambridge, Massachusetts, 02139, United States

[‡]University of Illinois, Urbana−Champaign, Illinois, 61801, United States

[§]Purdue University, West Lafayette, Indiana, 47907, United States

[▽]Università degli Studi di Pavia, Via Ferrata 1, 27100 Pavia, Italy

[⊥]Mettler−Toledo International, Inc., Columbia, Maryland 21046, United States

Supporting Information

ABSTRACT: The evolution of particle shape is an important consideration in many industrial crystallizations. This article describes the design of temperature-cycling experiments (between alternating positive and negative supersaturations) to substantially change crystal shape with only a small number of cycles. The growth and dissolution of monosodium glutamate crystals of varying shapes were monitored using in-process attenuated total reflection−Fourier transform infrared spectroscopy (ATR-FTIR), focused beam reflectance measurement (FBRM), particle vision and measurement (PVM), and off-line optical microscopy. The growth and dissolution kinetics were estimated in a multidimensional population balance model based on solute concentration and crystal dimension measurements. This model fitted the experimental data with a limited number of parameters of small uncertainty. In addition, with the estimated kinetic parameters, the model predicted the crystal size and shape distribution in a different temperature-cycling experiment reasonably well. In contrast to previous studies that have estimated kinetics along multiple crystal axes in mixed-tank crystallizers, this study implements dissolution terms in the multidimensional population balance model along multiple axes.

1. INTRODUCTION

A large proportion of crystallizations from solution produce rod-like crystals, which can cause problems in downstream process operations. One effective method for modifying the crystal shape and size is to introduce molecular additives,[1−3] which have the potential problem of contaminating the product. An alternative method of shape modification is to optimally control the supersaturation trajectory or by cycling between positive and negative supersaturations to take advantage of different relative dependencies along the crystal axes of growth and dissolution.[4−11] A very large change in the crystal shape has been reported with 20−80 temperature cycles, both theoretically and experimentally.[8,12] This article experimentally demonstrates that a large change in crystal size and aspect ratio is possible with a reduced number of temperature cycles (e.g., 3−6).

Many efforts have been directed toward the construction of multidimensional population balance models (PBMs) suitable for the design of process operations to optimize crystal shape.[9,13−22] These models require the estimation of growth kinetics along multiple axes, with most methods based on sampling the slurry during crystallization, or on employing imaging technology.[4,23−32] A commercial instrument that has been used for in situ measurement of the crystal shape distribution is particle vision and measurement (PVM).[33] Focused beam reflectance measurement (FBRM) is commonly available in crystallization laboratories, but it is not possible to construct an arbitrary two-dimensional crystal size distribution (2D CSD) from measurements of the chord length distribution (CLD) obtained via FBRM. The CLD data are not sufficiently informative for accurate quantitative correlation to a 2D CSD, even with a design limiting the variety of CSDs with a set seed mass and supersaturation profile.

To identify dissolution and growth kinetic parameters in a 2D population balance model (PBM), this article uses solute concentrations determined using ATR-FTIR spectroscopy[34−36] and mean crystal lengths and widths from microscope images.[17,37−40] Trends in mean crystal width, length, and aspect ratio in intermediate times were measured using FBRM. The initial crystal size distributions in the PBM were determined from PVM measurements. Compared to the previously published multidimensional PBMs, the PBM in this article includes dissolution kinetics. The PBM is used to predict the crystal size and shape distribution in a temperature-cycling experiment with a different supersaturation profile.

2. EXPERIMENTAL AND NUMERICAL METHODS

This section summarizes experimental methods for characterization of the solute concentration and mean length and width

Special Issue: David Himmelblau and Gary Powers Memorial

Received: March 17, 2013
Revised: January 2, 2014
Accepted: January 20, 2014
Published: January 20, 2014

   dx.doi.org/10.1021/ie400859d | Ind. Eng. Chem. Res. 2014, 53, 5325−5336

for monosodium glutamate (MSG) crystals in aqueous solution by attenuated total reflection−Fourier transform infrared (ATR-FTIR) spectroscopy, chemometrics, FBRM, PVM, and optical microscopy. Then, we describe a two-dimensional population balance model (PBM) for the growth and dissolution of rodlike crystals, and the numerical algorithms for simulation of the model and for estimation of the growth and dissolution kinetics along the length and width dimensions of the crystals.

2.1. Experimental Setup. The solute was monosodium glutamate (MSG, from Ajinomoto, with DSC and TGA data in Figures S1 and S2 in the Supporting Information), whose crystals are rodlike in shape. The solvent was deionized (DI) water. Within the experimental temperature range and solvent, MSG crystallizes as a monohydrate.[41] Crystallizations were carried out in two 100-mL cylindrical glass vessels were placed side by side in an EasyMax crystallization platform. Because of the inability to place all probes within one vessel (due to space limitations), one vessel had PVM (Lasentec V819L) and S-series FBRM probes and the other vessel had ReactIR and G-series FBRM probes. This study utilized chord length data measured every 10 s with the G-series (G400) FBRM probe and iC FBRM 4.2.65 Beta software. Infrared spectra for MSG in DI water were collected once every minute in a stirred crystallizer, using an in situ ReactIR probe with iC IR 4.2 software (ReactIR 15 FTIR reaction analysis system) with 256 scans collected for each spectrum and DI water at 25 °C used for the background spectrum. Metal overhead stirrers were continuously operated at rotational speed of 150−200 rpm, which was just enough to well suspend the crystals. The temperatures of both crystallizers were measured every 2 s and adjusted through the solid-state thermostat embedded in the EasyMax platform controlled with iControl EasyMax 4.1 software. Off-line optical images were taken of the crystal slurry or crystals obtained by vacuum filtration by polarized microscopes (Leica DM2500 and Zeiss Axiovert 200) with a digital camera (Leica DFC 400 Color).

2.2. Microscope Images for Measuring Mean Crystal Length and Width. During two temperature-cycling experiments, slurry samples of 2 mL were collected from the crystallizer at certain times during the cycles when the slurry was at the lowest temperature, to reduce potential size changes during the off-line measurement of the mean crystal length and width by optical microscope. The mean length and width of crystals were measured from the microscope images.

2.3. IR Calibration for Solute Concentration. The two crystallizers were cooled at a constant rate of 0.5 °C/min for different known MSG concentrations (Table 1) in 120 g of aqueous solution, while being measured with in situ ReactIR spectroscopy and FBRM. Each decrease in the solute concentration was achieved by dosing the solvent, followed by equilibration after measurements were taken for a higher concentration, all controlled with a procedure preset in the EasyMax software. The FBRM total counts per second were at very low levels throughout the calibration experiments, confirming that nucleation was negligible during these IR calibration experiments (that is, the metastable limit was not crossed).

IR absorbance spectra after DI water background subtraction and baseline offset were exported from the iC IR 4.2 software. Five chemometrics methods detailed by Togkalidou et al.[35] were applied to the absorbance spectra in the range 1200−1800 cm^{-1} with known solute concentrations and temperatures to construct a linear calibration model for measurement of the solute concentration:

$$C = \sum_{j=1200}^{1800} w_j a_j + w_T T + w_0 \quad (1)$$

where C is the solute concentration (g MSG/g water), a_j is the absorbance at frequency j (cm^{-1}), T is the temperature (°C), and w_j, w_T, and w_0 are regression coefficients. Representative infrared (IR) spectra and the regression coefficients are shown in Figure 1, with the equipment and procedures being the same as for other solute−solvent systems.[42,43] The calculations were carried out using in-house Matlab 5.3 code (The Mathworks, Inc., Natick, MA). Standard principal component regression with a noise level of 0.015 gave the smallest 95% prediction interval of ±0.0055 g/g solvent. The regression coefficient plot in Figure 1b does not show any spikes that would indicate overfitting, and is relatively flat except for frequencies where there are large peaks, as expected.

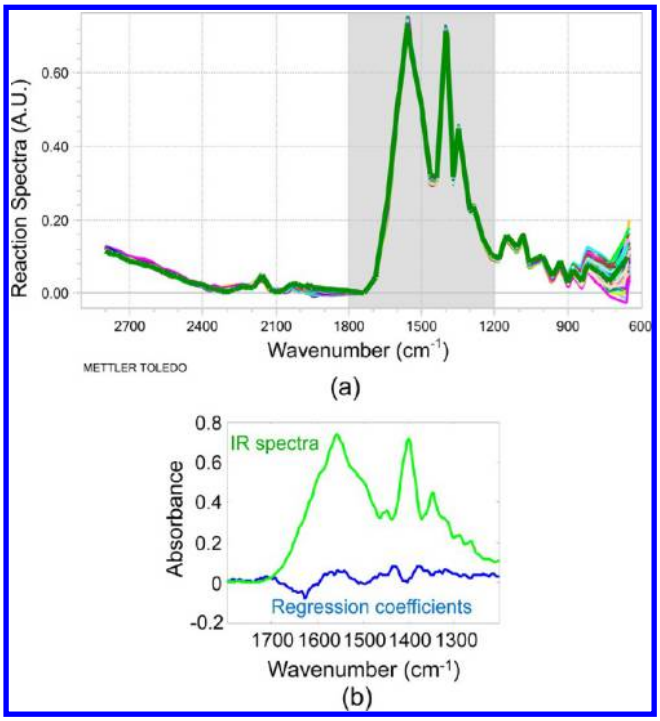

Figure 1. (a) Representative Fourier transform infrared (FTIR) spectra of MSG aqueous samples used for calibration. (b) Regression coefficients of the calibration model relating absorbance to solute concentration.

Table 1. ReactIR Calibration Samples for In Situ Solute Concentration Measurement

calibration sample	solute concentration (g/g solvent)	temperature range (°C)	number of spectra
Cs1	0.7937	65.0−48.3	34
Cs2	0.7576	55.0−37.9	35
Cs3	0.7246	44.9−32.1	26
Cs4	0.6944	35.0−22.7	25

2.4. Temperature-Cycling Experiments for Kinetics Estimation and Model Validation. The cycling experiment that produced the measurements of mean crystal length and

dx.doi.org/10.1021/ie400859d | Ind. Eng. Chem. Res. 2014, 53, 5325−5336

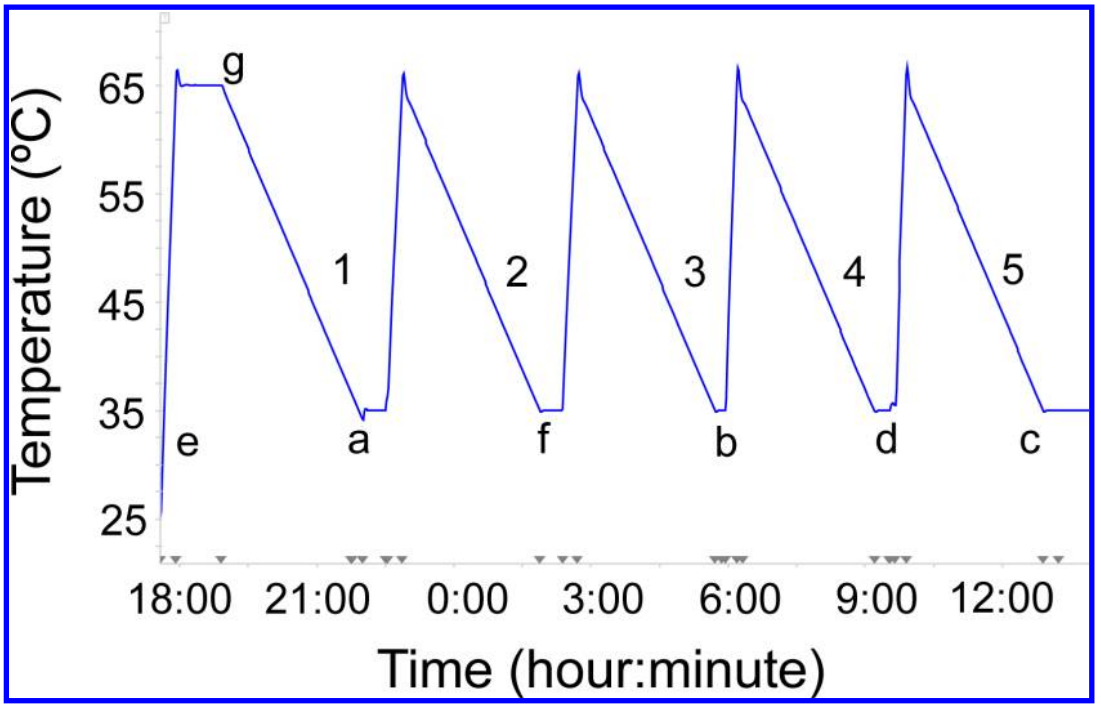

Figure 2. Temperature profile for the estimation temperature-cycling experiment (five cycles).

width and solute concentration used for kinetics estimation followed this procedure (Figure 2):

(1) Add 66.6 g of MSG (milled with IKA mill Werke MP 10) to 60 mL of DI water.
(2) Stir at 25 °C for 5 min.
(3) Heat to 65 °C at a rate of 2 °C/min.
(4) Hold for 1 h to fully equilibrate.
(5) Cool to 35 °C at a rate of 10 °C/h.
(6) Hold at 35 °C for 30 min.
(7) Heat to 65 °C at a rate of 2 °C/min.
(8) Repeat the cooling/hold/heating cycle in Steps 5−7 three more times before the end of the experiment.

The milling of the seed crystals to produce more surface area for growth did not change the hydration state of the MSG crystals (Figure S3 in the Supporting Information). The heating rate in Figure 2 was set high because dissolution kinetics are much faster than growth kinetics, which was observed in the preliminary experiments by observing the IR spectra abruptly stop changing when the temperature was held at a constant value after heating. The cooling rate was set to be just slow enough to suppress nucleation based on analysis of PVM and optical microscopy images collected during preliminary experiments.

Past studies have demonstrated a very large change in the crystal shape with 20−80 temperature cycles.[8,12] In this study, the temperature range was chosen to be much greater (65 °C − 35 °C = 30 °C) so that a large crystal mass dissolves and then grows during each cycle, to generate a larger change in crystal shape during each cycle. The very high heating rate during the dissolution state of each cycle, and the use of a cooling rate nearly as high as possible while avoiding nucleation, enable a larger number of cycles to be completed in the same time period.

The mean crystal length and width were validated in another temperature-cycling experiment that followed the same experimental procedure, but with 7 cycles, a lower temperature range, and no solute concentration measurement. These different experimental conditions were expected to lead to different amounts of change in crystal size and shape for the two experiments.

2.5. Simulation and Optimization Codes for Kinetics Estimation and CSD Prediction. Experimental data (e.g., size of time step, number of time steps, initial liquid concentration and solvent mass) were input to a Matlab simulation-optimization code that estimated kinetic parameters based on an initial estimate obtained from an initial set of simulation runs in which one parameter was changed at a time based on physical intuition on the effect of each parameter on the solute concentration and mean crystal length and width profiles. The two-dimensional (2D) PBM included size-dependent dissolution and growth terms,

$$\frac{\partial f}{\partial t} + \frac{\partial}{\partial L}(G_L f) + \frac{\partial}{\partial W}(G_W f) = 0 \qquad \text{for } S \geq 0$$
$$\frac{\partial f}{\partial t} - \frac{\partial}{\partial L}(D_L f) - \frac{\partial}{\partial W}(D_W f) = 0 \qquad \text{for } S < 0 \tag{2}$$

where f is the 2D population density, S the absolute supersaturation, and t the time. The growth and dissolution rates in the length L and width W directions are assumed to be 2D generalizations of the 1D equations,[44] i.e.,

$$G_L = k_{G_{L0}} \exp\left(-\frac{\Delta E}{RT}\right) S^{g_L}(1 + \delta_{G_L} L)$$
$$G_W = k_{G_{W0}} \exp\left(-\frac{\Delta E}{RT}\right) S^{g_W}(1 + \delta_{G_W} W)$$
$$D_L = \frac{k_{D_L}(-S)^{d_L}}{L^{\gamma}}$$
$$D_W = \frac{k_{D_W}(-S)^{d_W}}{W^{\gamma}} \tag{3}$$

dx.doi.org/10.1021/ie400859d | Ind. Eng. Chem. Res. 2014, 53, 5325−5336

and δ_{ij} and γ define size dependencies. The 2D PBM (eq 2) was combined with a solute mass balance and solved using a multidimensional method of characteristics algorithm.[45−48] All but six of the kinetic parameters were set to fixed values, as described in the caption to Table 2, with the remaining six parameters determined by applying successive quadratic programming to minimize the sum-of-squared-deviations between the model predictions and experiments,

$$\min_{\underline{\theta}\le\theta\le\bar{\theta}} \frac{1}{\sigma_C^2}\sum_{i=1}^{N_C}[C_{\text{measured}}(t_i) - C_{\text{model}}(t_i;\theta)]^2 + \sum_{k=1}^{4}\frac{1}{\sigma_{L,k}^2}[L_{\text{measured}}(t_k) - L_{\text{model}}(t_k;\theta)]^2 + \sum_{k=1}^{4}\frac{1}{\sigma_{W,k}^2}[W_{\text{measured}}(t_k) - W_{\text{model}}(t_k;\theta)]^2 \quad (4)$$

where

$$\theta = [\ln k_{G_{W0}} \quad \ln k_{G_{L0}} \quad g_W \quad g_L \quad \ln k_{D_W} \quad \ln k_{D_L}]^T \quad (5)$$

is the vector of fitted model parameters, N_C is the number of concentration measurements, σ is the standard deviation of each measurement error, and the subscripts C, L, and W refer to the solute concentration and mean crystal length and width, respectively. These coefficients weigh the relative confidence in the measurements of solute concentration and mean crystal length and width, to produce parameter estimates that are unbiased with minimum variance assuming that the errors have zero expectation and are uncorrelated with each other and the independent variables.[49]

Uncertainties in the parameter estimates were quantified using standard methods whose applications to crystallization are well-established.[50] With the vector of predicted variables

$$\underline{Y} = [C_1 \quad C_2 \quad \cdots \quad C_{N_C} \quad L_1 \quad L_2 \quad L_3 \quad L_4 \quad W_1 \quad W_2 \quad W_3 \quad W_4]^T \quad (6)$$

the sensitivity matrix for this system is

$$\underline{\underline{F}} = \left.\frac{\partial \underline{Y}}{\partial \theta}\right|_{\theta^*} = \begin{bmatrix} \frac{\partial C_1}{\partial \ln k_{G_{W0}}} & \frac{\partial C_1}{\partial \ln k_{G_{L0}}} & \frac{\partial C_1}{\partial g_W} & \frac{\partial C_1}{\partial g_L} & \frac{\partial C_1}{\partial \ln k_{D_W}} & \frac{\partial C_1}{\partial \ln k_{D_L}} \\ \frac{\partial C_2}{\partial \ln k_{G_{W0}}} & \frac{\partial C_2}{\partial \ln k_{G_{L0}}} & \frac{\partial C_2}{\partial g_W} & \frac{\partial C_2}{\partial g_L} & \frac{\partial C_2}{\partial \ln k_{D_W}} & \frac{\partial C_2}{\partial \ln k_{D_L}} \\ \vdots & \vdots & \vdots & \vdots & \vdots & \vdots \\ \frac{\partial C_{N_C}}{\partial \ln k_{G_{W0}}} & \frac{\partial C_{N_C}}{\partial \ln k_{G_{L0}}} & \frac{\partial C_{N_C}}{\partial g_W} & \frac{\partial C_{N_C}}{\partial g_L} & \frac{\partial C_{N_C}}{\partial \ln k_{D_W}} & \frac{\partial C_{N_C}}{\partial \ln k_{D_L}} \\ \frac{\partial L_1}{\partial \ln k_{G_{W0}}} & \frac{\partial L_1}{\partial \ln k_{G_{L0}}} & \frac{\partial L_1}{\partial g_W} & \frac{\partial L_1}{\partial g_L} & \frac{\partial L_1}{\partial \ln k_{D_W}} & \frac{\partial L_1}{\partial \ln k_{D_L}} \\ \vdots & \vdots & \vdots & \vdots & \vdots & \vdots \\ \frac{\partial L_4}{\partial \ln k_{G_{W0}}} & \frac{\partial L_4}{\partial \ln k_{G_{L0}}} & \frac{\partial L_4}{\partial g_W} & \frac{\partial L_4}{\partial g_L} & \frac{\partial L_4}{\partial \ln k_{D_W}} & \frac{\partial L_4}{\partial \ln k_{D_L}} \\ \frac{\partial W_1}{\partial \ln k_{G_{W0}}} & \frac{\partial W_1}{\partial \ln k_{G_{L0}}} & \frac{\partial W_1}{\partial g_W} & \frac{\partial W_1}{\partial g_L} & \frac{\partial W_1}{\partial \ln k_{D_W}} & \frac{\partial W_1}{\partial \ln k_{D_L}} \\ \vdots & \vdots & \vdots & \vdots & \vdots & \vdots \\ \frac{\partial W_4}{\partial \ln k_{G_{W0}}} & \frac{\partial W_4}{\partial \ln k_{G_{L0}}} & \frac{\partial W_4}{\partial g_W} & \frac{\partial W_4}{\partial g_L} & \frac{\partial W_4}{\partial \ln k_{D_W}} & \frac{\partial W_4}{\partial \ln k_{D_L}} \end{bmatrix} \quad (7)$$

where θ^* is the vector of optimal parameter estimates (values listed in Table 2). Each element of $\underline{\underline{F}}$ was calculated by the two-point central finite difference formula and used to construct an estimate of the parameter covariance matrix,

$$\underline{\underline{V_\theta^{-1}}} = \underline{\underline{F}}\,\underline{\underline{V_\varepsilon^{-1}}}\,\underline{\underline{F}}^T \quad (8)$$

given the measurement error covariance matrix,

$$\underline{\underline{V_\varepsilon}} = \text{diag}(\sigma_C^2 \underline{\underline{I_{N_C}}}, \sigma_{L,1}^2, \sigma_{L,2}^2, \sigma_{L,3}^2, \sigma_{L,4}^2, \sigma_{W,1}^2, \sigma_{W,2}^2, \sigma_{W,3}^2, \sigma_{W,4}^2) \quad (9)$$

Table 2. Kinetic Parameters Estimated from Fitting Data from the Estimation Temperature-Cycling Experiment or Set with Justifications[a]

parameter	optimal value	units	fitted or fixed parameter?
$k_{G_{L0}}$	6.4×10^{13}	μm (g water)^2/[min (g MSG)^2]	fitted
g_L	2.00	dimensionless	fitted
g_{G_L}	0	$1/\mu$m	fixed
$k_{G_{W0}}$	2.3×10^{13}	μm (g water)^2/[min (g MSG)^2]	fitted
g_W	2.00	dimensionless	fitted
δ_{G_W}	0	$1/\mu$m	fixed
k_{D_L}	4.4×10^6	μm^2 (g water)/[min (g MSG)]	fitted
k_{D_W}	1.6×10^6	μm^2 (g water)/[min (g MSG)]	fitted
d_L	1	dimensionless	fixed
d_W	1	dimensionless	fixed
γ	1	dimensionless	fixed
ΔE	71.24	kJ/mol	fixed

[a]The lower and upper bounds for the growth exponents g_L and g_W were 1 and 2, as specified by theory.[50] The dissolution exponents d_L and d_L were set equal to 1, to be consistent with the assumption of mass-transfer-limited dissolution,[53] and the size dependencies in the growth rates (δ_{G_L} and δ_{G_W}) were set to zero, since nonzero values did not significantly improve the fit to data. The average activation energy (71.24 kJ/mol) in G_W and G_L expressions was estimated from ref 34. The value of γ was selected to capture the trends in the increase in mean crystal length and width (see Figure 9b). Varying the value of the dependency of the dissolution rate on the crystal dimensions (γ in eq 3) above 1 did not affect the quality of fit much (comparison not shown). Although it could be argued from physical grounds that the dissolution rate in the length direction should be better modeled as being dependent on the size in the width direction and vice versa, swapping these dependencies did not improve the quality of the model's fit to data.

3. RESULTS AND DISCUSSION

3.1. Evolution of Crystal Dimensions for the Temperature-Cycling Experiments. In the estimation temperature-cycling experiment, the FBRM statistics had not converged to a stable oscillation even after five cycles (Figure 3), with the square-weighted mean chord length at the end of each cycle increasing with cycle number, indicating that each cycle continues to increase the size of the crystals. The increase in the ratio of the mean cube-weighted and square-weighted mean chord length (blue line in Figure 3) is associated with a change in the mean aspect ratio (see Table 3). The trends agreed with the off-line microscope images (see Figure 4) and PVM images (see Figure 5), which clearly showed that each cycle continued

dx.doi.org/10.1021/ie400859d | Ind. Eng. Chem. Res. 2014, 53, 5325−5336

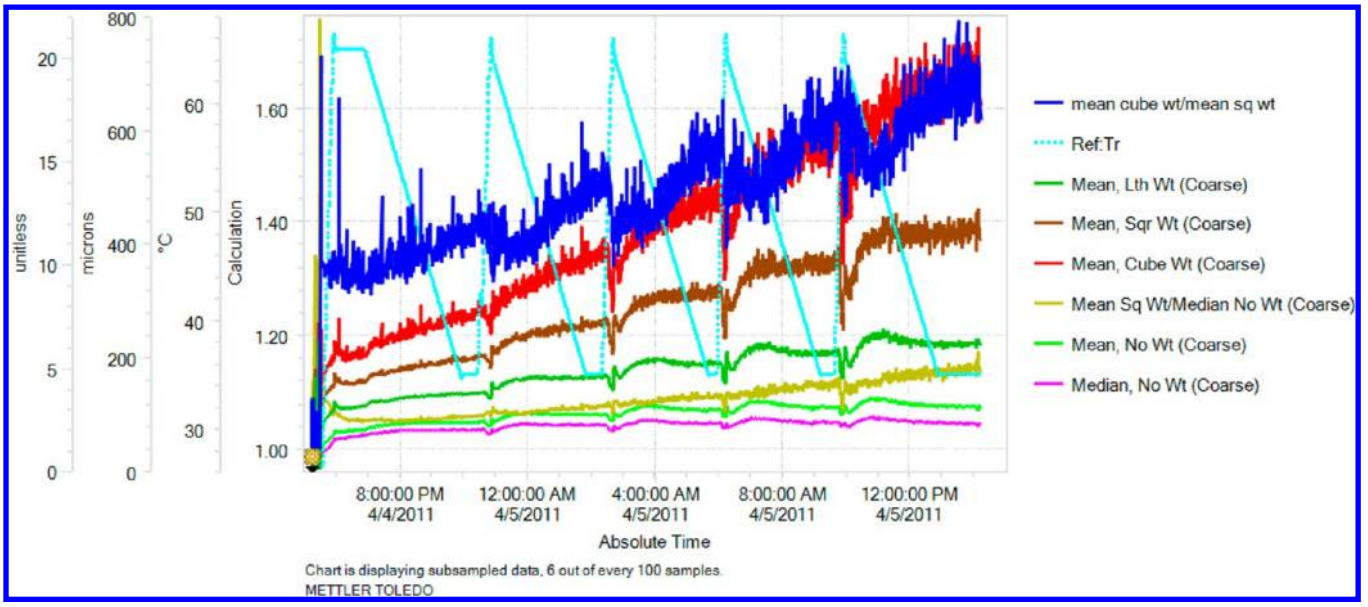

Figure 3. Mean chord length for various length weightings (none, length, square, and cubic) for the estimation temperature-cycling experiment. All of the mean chord lengths show a periodic change following temperature cycles (cyan line) starting from the plateau of the first cycle (when the slurry is equilibrated). Various length-weighted average chord lengths indicate that the crystal dimensions increase as the cycle number increases, and the ratio of mean cube-weighted to square-weighted mean sizes indicate that the mean aspect ratio increases as the cycle number increases. To better visualize the trends and variations, the chart displays 6 out of every 100 data points.

Table 3. Mean Aspect Ratio and Standard Deviations from Microscope Measurements for the Five-Cycle Experiment[a]

	mean aspect ratio	standard deviation
cycle 1a	2.555	0.076
cycle 3b	3.244	0.159
cycle 4d	3.936	0.187
cycle 5c	4.660	0.243

[a]The sampling points (e.g., 1a, 3b) are shown in Figure 2.

to increase the mean crystal length, width, and aspect ratio. The same trends are seen in the FBRM statistics and off-line microscope images for the validation temperature-cycling experiment (see Figures 6 and 7). While past modeling results for temperature cycling of a single crystal indicated that the crystal shape can significantly continue to change after many cycles,[8,10] an interesting aspect of the experimental data for the crystal size and shape distribution in Figures 3−7 is that deep cycling enables the mean crystal dimensions to significantly increase at the end of *each cycle*.

We will see, in the solute concentration measurements in section 3.2, that the solute concentration at the lowest temperature, when the slurry samples are collected, increases little from one cycle to the next. Since the total quantity of solute molecules is constant, the total mass of crystals when samples are collected changes slowly with cycle number, which suggests that the increase in the crystal dimensions after each cycle is mostly explained by a reduction in the total number of crystals during each dissolution step. For this reduction to occur, a significant fraction of the crystals becomes small enough to completely dissolve in each cycle. This observation implies that the CSD must become broader during each cycle, which can only occur in the two-dimensional population balance model (PBM(2)) if the growth and/or dissolution rates are size-dependent. Most reported dissolution rate expressions are size-dependent,[44] whereas most reported growth rates are size-independent,[50] so these assumptions were made in this article.

3.2. Evolution of Crystal Dimensions and Solute Concentration for the Estimation Temperature-Cycling Experiment. The solute concentration during the estimation temperature-cycling experiment is shown in Figure 8. For the first cycle, the temperature was held constant immediately after the first heating ramp, to enable a qualitative assessment of the dissolution rate. The solution concentration reaches a constant value shortly after the temperature is held constant, indicating that the dissolution rate is fast enough for the solute concentration to quickly reach steady-state (and, hence, the saturated concentration).

The solute concentration at the highest temperature (~65 °C) is almost the same for each cycle (Figure 8, where each narrow peak arises from overshooting of the temperature at each transition between heating to cooling), and the supersaturation is largely consumed before the next heating stage (Figure 9a). Given that the solute conditions are essentially the same at the start of each cooling stage, the increase of solute concentration at the end of each cooling stage (35 °C, see Figure 8), must be associated with a decrease in the overall crystal mass grown during each cycle. As the average supersaturation during each cooling stage increases (thus the growth rate increases[51]) with cycle number (Figure 9a), the decrease in the overall crystal mass grown is explained by a reduction in the amount of crystal surface area in each subsequent cycle. This analysis is consistent with a decrease in the total number of crystals at the end of each cycle, as the crystals become larger, as seen in the FBRM statistics and PVM and optical microscopy images (Figures 3−5).

The use of the in situ measurements of the solute concentration and crystal mean length and width to estimate the dissolution and growth kinetics is described next.

3.3. Simulation and Prediction of CSDs with Estimated Kinetic Parameters. The two-dimensional

dx.doi.org/10.1021/ie400859d | Ind. Eng. Chem. Res. 2014, 53, 5325−5336

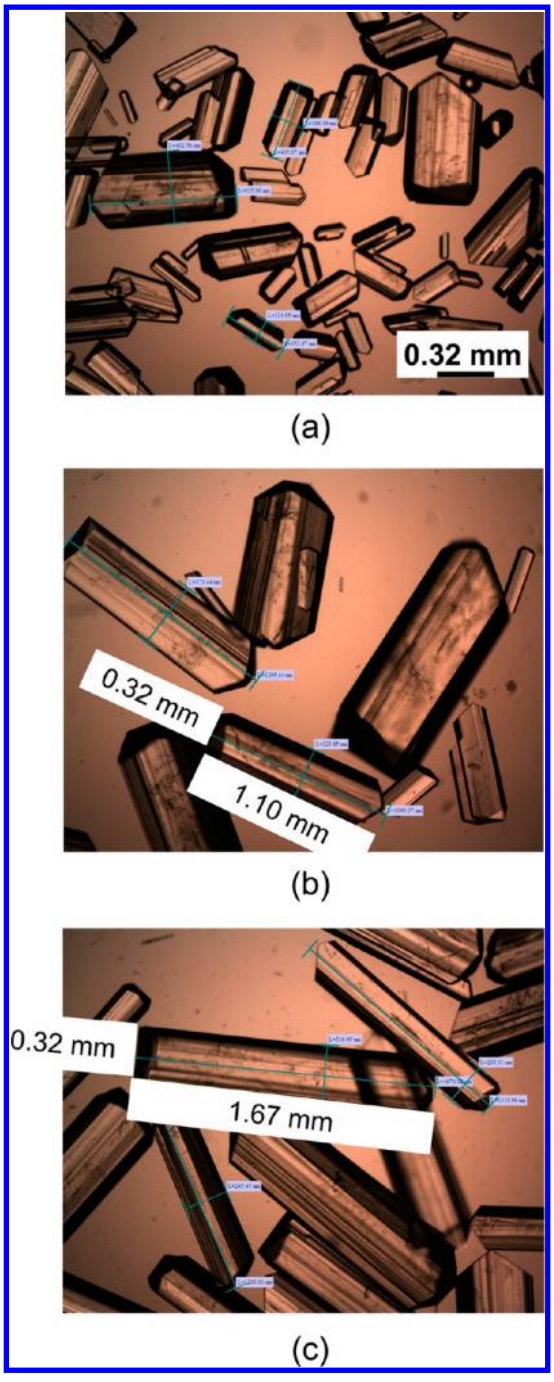

Figure 4. Microscopy images (with polarizers) of MSG slurry for samples collected at 35 °C in the estimation temperature-cycling experiment at (a) cycle 1a, (b) cycle 3b, and (c) cycle 5c. The timing of the sampling points is shown in Figure 2.

dissolution and growth kinetic parameters determined by the application of least-squares estimation to the data from the estimation temperature-cycling experiment are reported in Table 2, with comparisons between model predictions and experiments in Figure 9. The estimated parameters for the growth and dissolution rates in Table 2 have values that are consistent with theory.[44,51] Approximately half of the model parameters were set based on theory or experimental studies by other groups, as described in the caption of Table 2, and the simulation parameters are given in Table 4. The solute concentration from the PBM (eq 2) tracks the experimental

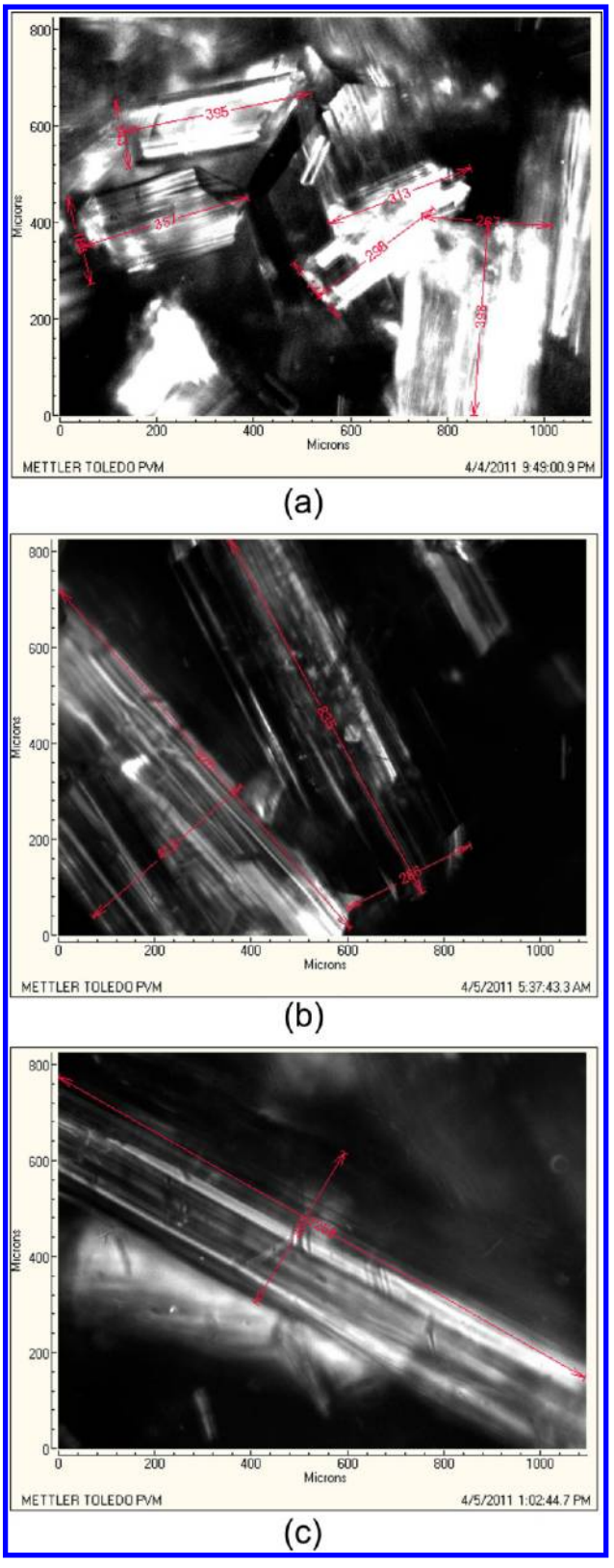

Figure 5. PVM images of MSG slurry at 35 °C in the estimation temperature-cycling experiment at (a) cycle 1a, (b) cycle 3b, and (c) cycle 5c. The timing of the measurement points is shown in Figure 2. The PVM images show that crystals grow larger as the cycle number increases, with some crystals growing larger than the image frame of PVM, such as in the fifth cycle. No secondary nuclei were observed in any of the PVM images collected during the experiments.

dx.doi.org/10.1021/ie400859d | Ind. Eng. Chem. Res. 2014, 53, 5325−5336

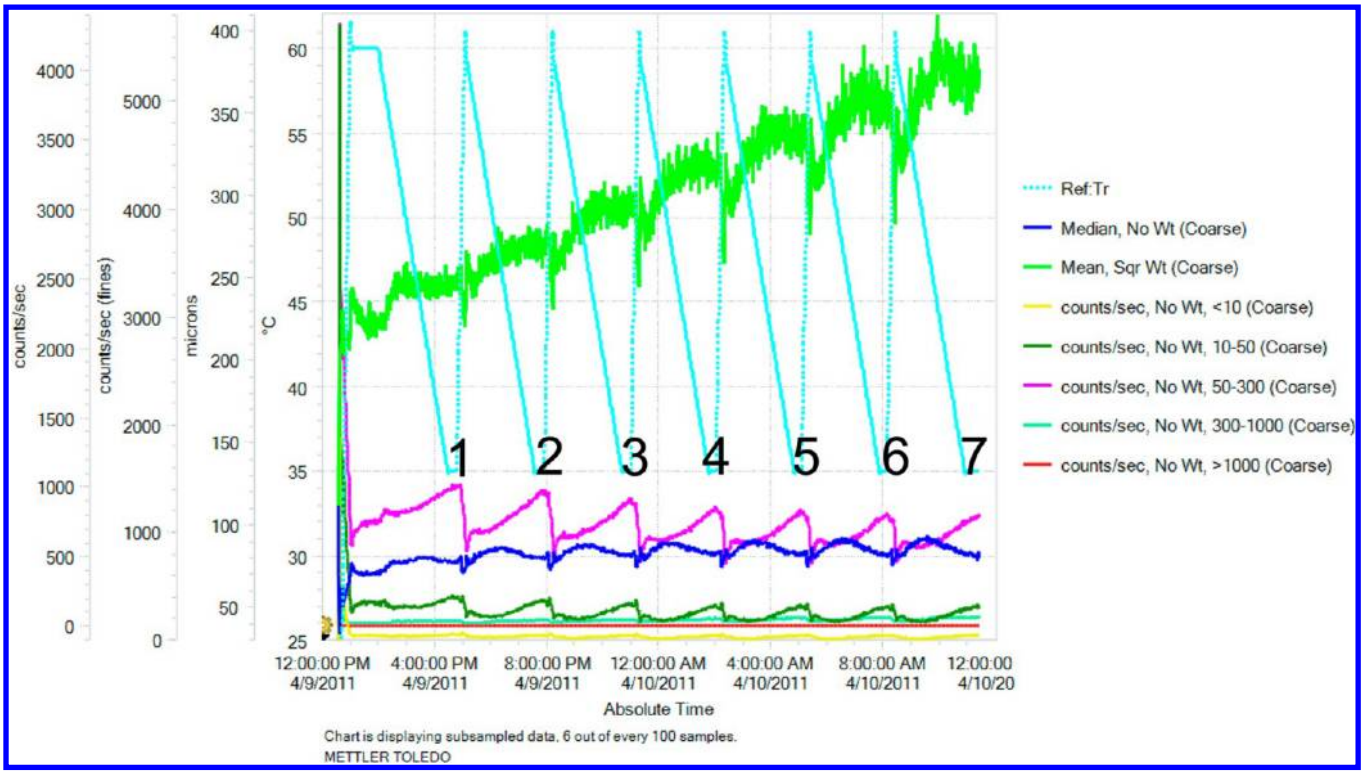

Figure 6. G400 FBRM (macro mode, which was called "coarse mode" in earlier versions of the FBRM software) counts-per-second statistics and temperature for the validation temperature-cycling experiment with samples collected at the end of the first, second, third, and seventh cycles (at 35 °C, timing of the four sampling points shown with cycle numbers). The validation experiment shows periodic changes in FBRM statistics as the temperature cycles, with a decrease in the measured number of smaller chord lengths (<300 μm) and an increase in mean square-weight size with cycle number.

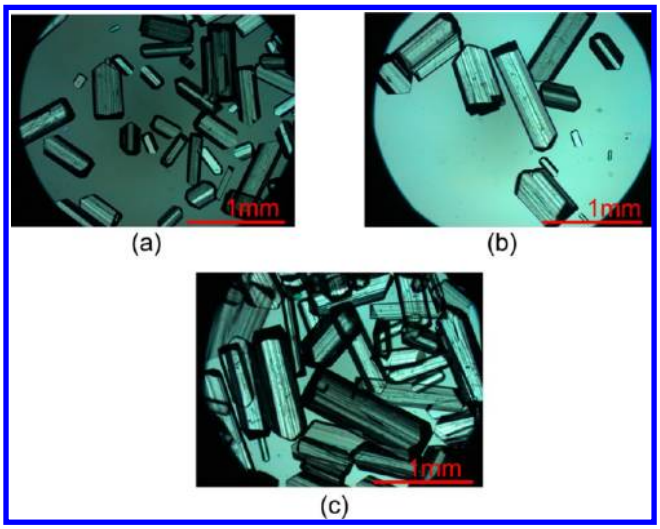

Figure 7. Microscopy images (with polarizers) of slurry of MSG crystals in aqueous solution for the validation temperature-cycling experiment at the end of (a) cycle 1, (b) cycle 3, and (c) cycle 7.

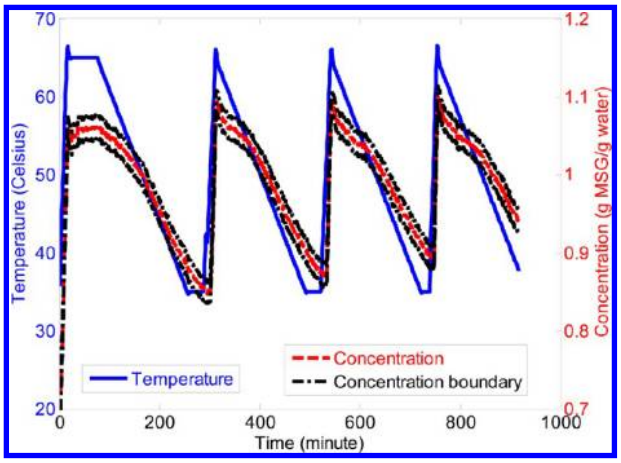

Figure 8. Solute concentration profile over time for the estimation temperature-cycling experiment. The time range covers the first four cycles. Beyond that time range (after point 4g in Figure 2), there was no FTIR equipment available. The distance along the vertical axis between red and black lines is σ_C in eq 4, which is the predicted standard deviation of solute concentration.

value, including the slow increase in the minimum solute concentration in each cycle (Figure 9a). The mean crystal length and widths from the model also track the optical microscopy measurements quite closely through all of the cycles, with somewhat larger deviations for the ratio of the mean length and mean width (Figure 9b).

The kinetic parameters in Table 2 were used to predict the mean crystal length and width (Figure 10) in another temperature-cycling experiment (e.g., the seven-cycle validation experiment, detailed in section 2.4 and Table 5). The predictions closely track the experimental data throughout the temperature cycles (Figure 10), except at the seventh cycle, which is consistent with the accumulation of the effects of model uncertainties on model predictions that would be expected in any process that has states whose values continue to drift over time. The mean crystal length prediction is especially accurate, with negligible prediction error for cycles 1,

dx.doi.org/10.1021/ie400859d | Ind. Eng. Chem. Res. 2014, 53, 5325−5336

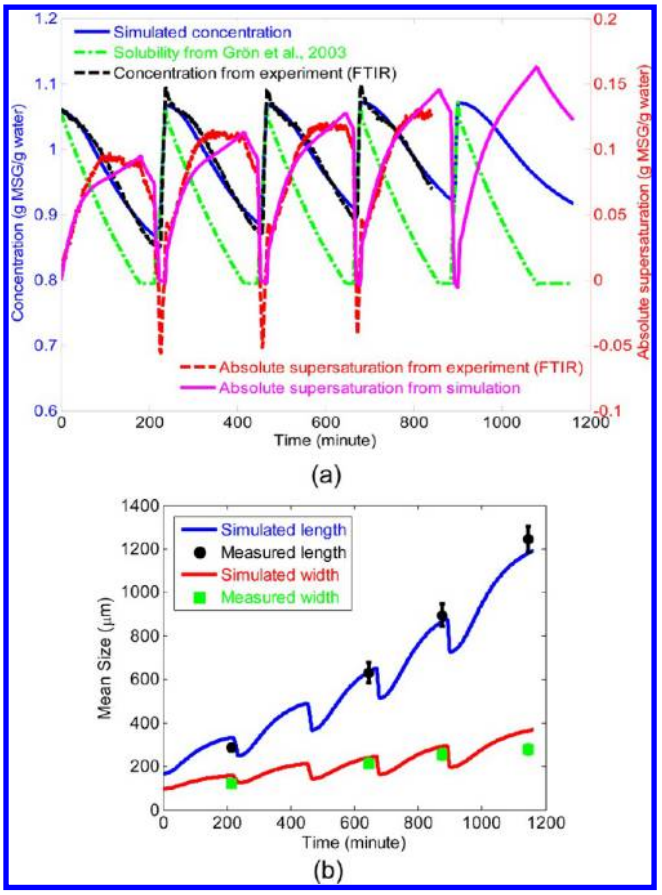

Figure 9. Comparison between experimental data and model predictions using the kinetic parameters in Table 2 for the estimation temperature-cycling experiment for (a) solute concentration and absolute supersaturation (the solubility, which is computed from an expression in ref 34. based on the implemented temperature, uses the same vertical axis as the solute concentration), and (b) mean crystal length (black circle denotes the experiment; blue line denotes the model) and width (green square denotes the experiment; red line denotes the model).

Table 4. Parameters Used in the Numerical Simulation of the Population Balance Model (PBM) (eq 2) in the Estimation Temperature-Cycling Experiment

variable	description	value
Δt	time step	0.05 min
ΔW	mesh size for the width	5.0 μm
ΔL	mesh size for the length	5.0 μm
$C(0)$	initial solute concentration	1.0558 g MSG/g water
M_s	mass of solvent (water)	begins at 60.0 g
	times at which a slurry sample was collected	215, 645, 875, 1145 min
T	real-time temperature	35.0–65.0 °C
	number of temperature points	1162

2, and 3 and <10% prediction error at cycle 7. The mean crystal width and the length-to-width ratio have larger deviations. The crystal size distributions at the sampling times were also calculated (see Figures 11 and 12) based on the estimated kinetic parameters (Table 2). The CSDs from the PBM grow wider with cycle number, which is consistent with having size-dependent dissolution rates in the model, and consistent with experimental measurements (Table 6). The trends in mean

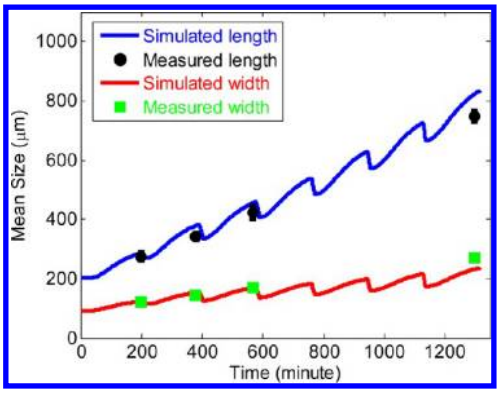

Figure 10. Comparison between experimental data and model predictions using the kinetic parameters in Table 2 for the estimation in the validation temperature-cycling experiment (seven cycles) for the mean crystal length (black circle denotes the experiment; blue line denotes the model) and width (green square denotes the experiment; red line denotes the model). The model expected errors in the mean crystal length and width are reported later in Table 9. The measurement error bars in the plot are the sample standard deviations computed by resampling the crystal size measurements.

Table 5. Parameters Used in the Numerical Simulation of the Population Balance Model (eq 2) in the Validation Temperature-Cycling Experiment

variable	description	value
Δt	time step	0.05 min
ΔW	mesh size for the width	5.0 μm
ΔL	mesh size for the length	5.0 μm
$C(0)$	initial solute concentration	1.0024 g MSG/g water
M_s	mass of solvent (water)	begins with 60.0 g
	times at which a slurry sample was collected	199, 379, 567, 1297 min
T	real-time temperature	35.0–60.0 °C
	number of temperature points	1318

width, length, and aspect ratio in Figure 10 and Table 7 agree with FBRM CLD data (Figure 6).

3.4. Parameter Estimation and Accuracy Quantification for the Population Balance Model. The parameter error estimates in Table 8 were obtained from eqs 4–9, using σ_C = 0.01 g MSG/g water and σ_L and σ_W in Figure 9b, based on the experimental data from the single temperature-cycling estimation experiment. Such parameter error estimates should always be taken as being underestimates, since the statistical assumptions that the errors have zero expectation and are uncorrelated with each other and the independent variables[49] almost never exactly hold in practice. In particular, the derivation of a first-principles model always includes some simplifying assumptions that do not exactly hold, such as perfect spatially uniform mixing, in which case the statistical assumptions will not hold exactly. Such parameter uncertainty estimates have been found to be useful in past crystallization studies,[11,50] and so are discussed here with those caveats in mind. A direct comparison to error estimates in past studies is appropriate as the statistical assumptions made in this article are the same.

From the single estimation temperature-cycling experiment, the estimated 95% confidence intervals for the prefactor of each growth rate in Table 8 are smaller than values reported in past studies that employed up to four batch experiments.[52] The single cycling experiment collects experimental data for a longer

dx.doi.org/10.1021/ie400859d | Ind. Eng. Chem. Res. 2014, 53, 5325–5336

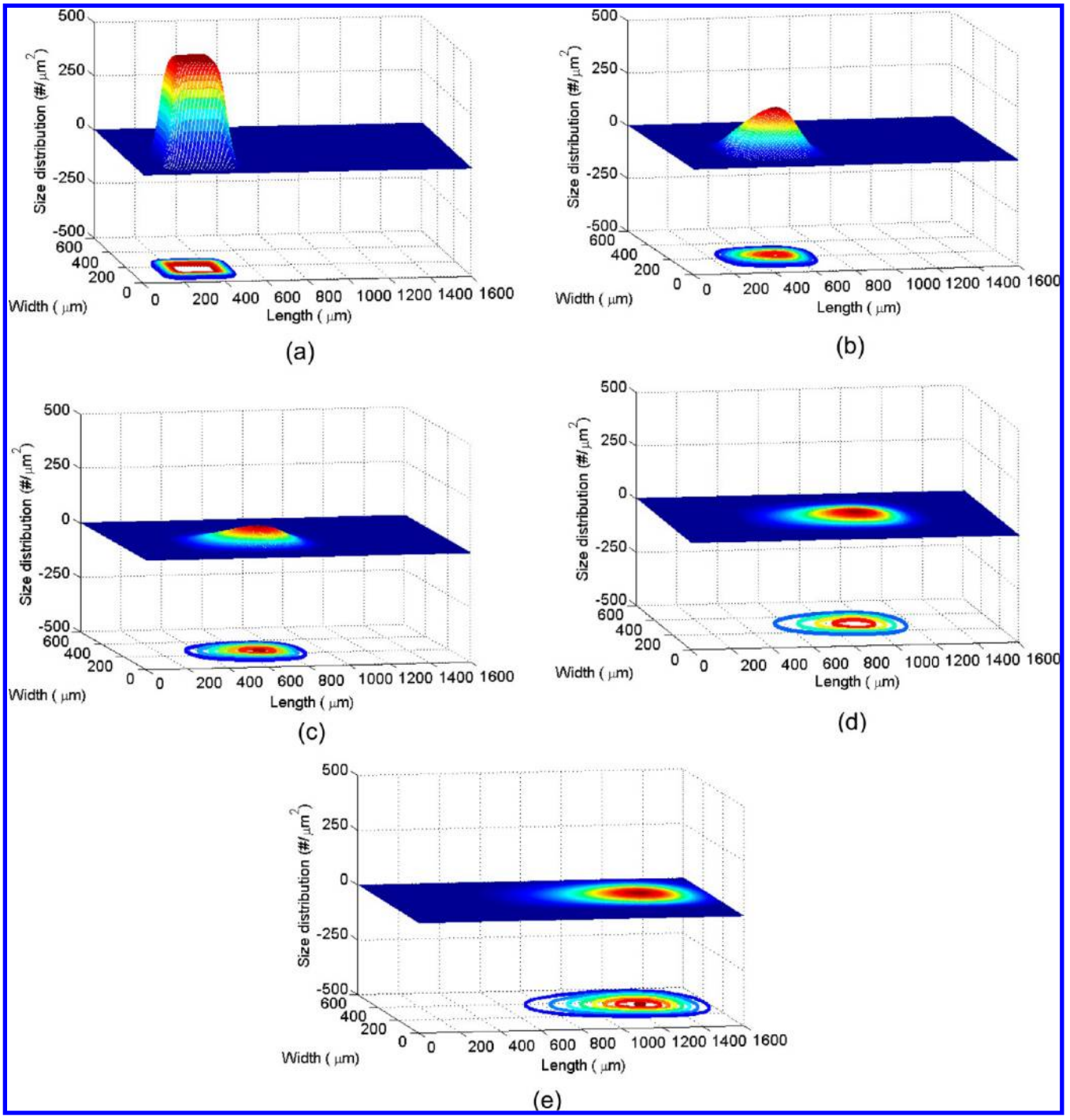

Figure 11. Crystal size distributions $f(L,W,t)$ of MSG slurry from model simulation using the kinetic parameters in Table 2 for the five-cycle estimation temperature-cycling experiment, with the points as in Figure 2: (a) cycle 1a, (b) cycle 2f, (c) cycle 3b, (d) cycle 4d, and (e) cycle 5c.

period of time than most batch experiments, and was designed to have positive supersaturation with significant growth rate occurring for >90% of the entire time period (see Figure 9a), hence producing data that is highly informative for growth rate estimation. The estimated 95% confidence intervals for the growth exponents are similar in magnitude to past studies.[52] The uncertainties in the dissolution rate constants are higher, up to 10%, which is quite accurate considering that the solute concentration closely follows the solubility curve during dissolution. The dissolution kinetics are so fast that the supersaturation is never far from zero during dissolution, so the uncertainties in the dissolution rate constants are larger than for the parameters in the growth rate expressions.

3.5. Comparison of Population Balance Model Predictions with Data from Validation Experiments. The small parametric uncertainties in Table 8 provide some confidence that the model predictions could be accurate enough to be used for design purposes. To make a more-informed assessment, the parameter covariance matrix was also used to estimate the accuracy of the model predictions for the validation seven-cycle experiment. The parameter covariance matrix, $\underline{\underline{V_\theta}}$, remains the same, while the sensitivity matrix is

dx.doi.org/10.1021/ie400859d | Ind. Eng. Chem. Res. 2014, 53, 5325−5336

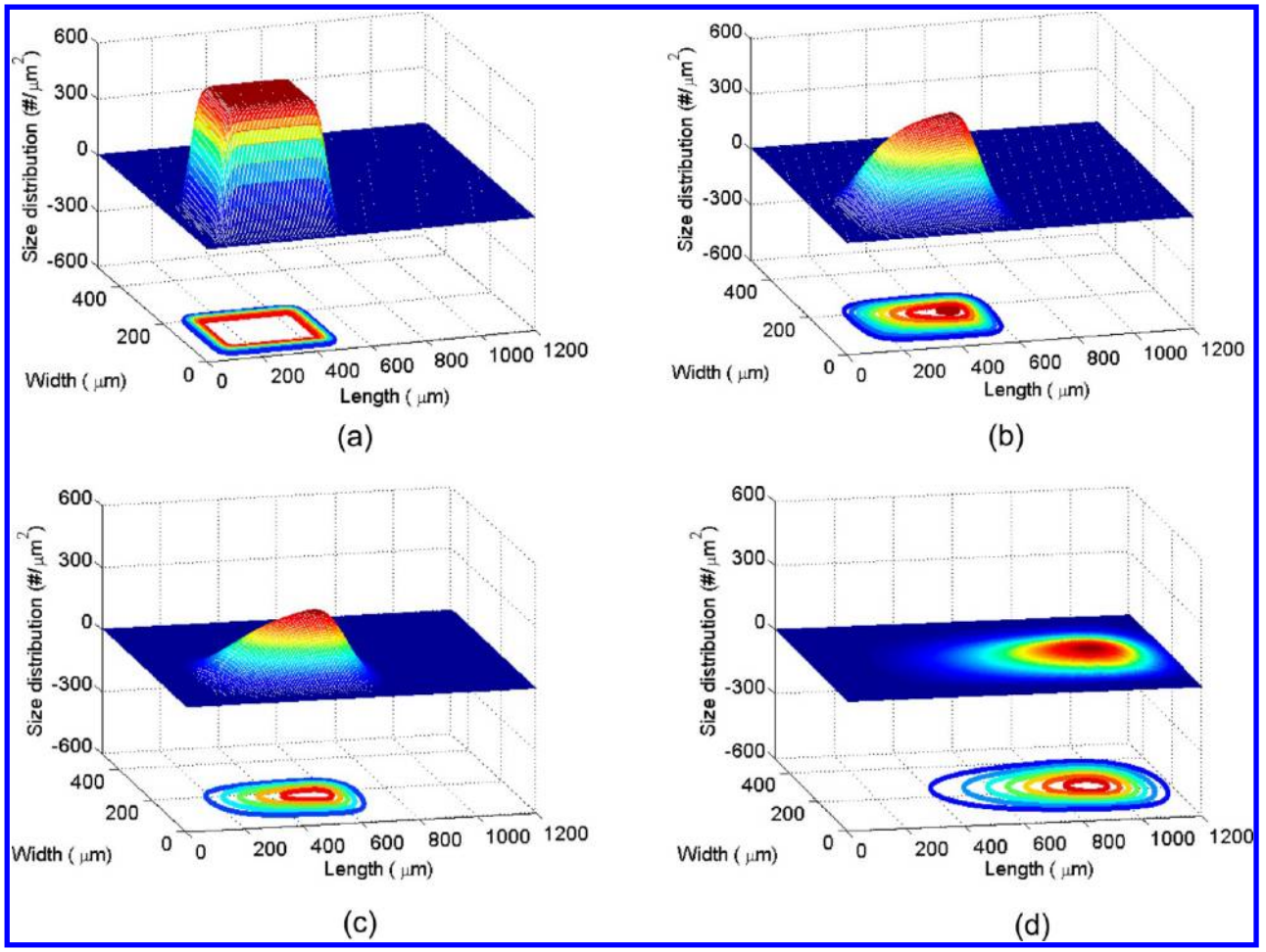

Figure 12. Crystal size distributions $f(L,W,t)$ of MSG slurry from model simulation using the kinetic parameters in Table 2 for the seven-cycle validation temperature-cycling experiment at the end of cycles, with the points as in Figure 6: (a) cycle 1, (b) cycle 2, (c) cycle 3, and (d) cycle 7.

Table 6. Crystal Length and Width Measurement from the Seven-Cycle Validation Experiment[a]

cycle number	minimum width (μm)	maximum width (μm)	minimum length (μm)	maximum length (μm)	range of width (μm)	range of length (μm)	number of crystals
1	17.0	345.3	38.0	1056.5	328.3	1018.5	201
2	25.6	389.8	36.9	1295.5	364.2	1258.6	287
3	26.8	474.8	81.0	1176.7	448.0	1095.7	138
7	40.2	651.2	160.5	1505.2	611.0	1344.7	187

[a]The cycle numbers are defined in Figure 3.

Table 7. Mean Aspect Ratio and Standard Deviations from Microscope Measurements for the Seven-Cycle Experiment[a]

	mean aspect ratio	standard deviation
Cycle 1	2.349	0.064
Cycle 2	2.399	0.050
Cycle 3	2.622	0.059
Cycle 7	2.835	0.053

[a]The sampling points are defined in Figure 6.

specific for each experiment. The sensitivity matrix for the seven-cycle experiment, $\underline{\underline{F}}_7$, was calculated using the same central finite difference method. The prediction error covariance matrix $\underline{\underline{V}}_Y$ was calculated from $\underline{\underline{V}}_Y = \underline{\underline{F}}_7^T \underline{\underline{V}}_\theta \underline{\underline{F}}_7$. The diagonal elements of $\underline{\underline{V}}_Y$ include the standard deviations of mean crystal length ($\sigma_{L,7}$) and width ($\sigma_{W,7}$) from the model prediction, all of which are listed in Table 9. The 95% prediction intervals for the predicted mean crystal length and width are estimated to be $\pm$12.5 μm and $\pm$2.5 μm, respectively, at cycle 7, suggesting that the difference between the model predictions and experimental data in Figure 10 is more likely to be due to uncertainties in the measurements rather than uncertainties in the model predictions.

CONCLUSIONS

Temperature-cycling experiments were designed in which the mean crystal dimensions and aspect ratio significantly increased at the end of each cycle, in a much smaller number of cycles than in previous studies.[8,12] Dissolution and growth kinetics in a population balance model were estimated along the length and width directions for rod-shaped crystals based on experimental data from commercial instrumentation applied to a single experiment in which the temperature cycles. The

dx.doi.org/10.1021/ie400859d | Ind. Eng. Chem. Res. 2014, 53, 5325−5336

Table 8. Estimated Confidence Intervals for Each Parameter Estimate in $\underline{\theta}^a$

parameter	optimal value	lower bound	upper bound
ln $k_{G_{W0}}$	30.78	30.72	30.84
ln $k_{G_{L0}}$	31.79	31.76	31.82
g_W	2.00	1.97	2.03
g_L	2.00	1.98	2.02
ln k_{D_W}	14.3	12.9	15.6
ln k_{D_L}	15.3	14.0	16.6

[a]As determined from Montgomery and Runger.[54] $\underline{\theta}$ is calculated from the expression $\underline{\theta} = \theta_i^* - t_{\alpha_t/2,\mathrm{DOF}}(V_{\theta,ii})^{1/2} \le \theta_i \le \theta_i^* + t_{\alpha_t/2,\mathrm{DOF}}(V_{\theta,ii})^{1/2}$, where $t_{\alpha_t/2,\mathrm{DOF}}$ is the Student t-distribution and DOF represents the degrees of freedom (DOF = 842 + 4 + 4 − 6 = 844; N_c = 842). For a confidence level of $100(1 - \alpha_t)\%$ = 95%, the value of t is 1.960. A confidence hyper-ellipsoid cannot be plotted, because $\underline{\theta}$ has six dimensions.

Table 9. Standard Deviation of the Mean Crystal Length and Width Predicted by the Model with Its Uncertainty Description, with the Time Points Being the Same as Given in Figure 12[a]

	Standard Deviations	
time point	mean crystal length, $\sigma_{L,7}$ (μm)	mean crystal width, $\sigma_{W,7}$ (μm)
cycle 1	1.7249	0.4516
cycle 2	2.8045	0.4993
cycle 3	3.0404	0.4663
cycle 7	6.2465	1.2851

[a]The prediction errors are much smaller than the noise in the mean crystal length and width measurements, so only bars on the estimated experimental measurement noise are shown in Figures 9 and 10.

outputs of the population balance model (eq 2) based on the minimum-variance kinetic parameter estimates tracked well the experimentally measured mean crystal dimensions and solute concentrations. With the same parameter estimates, the model predicted the crystal dimensions for another temperature-cycling experiment reasonably well (see Figure 10). Both this observation and uncertainty analysis suggested that growth and dissolution rates estimated in a single temperature-cycling experiment might be suitable for designing a temperature-cycling protocol for optimizing the size and shape of the product crystals.

■ ASSOCIATED CONTENT

Ⓢ Supporting Information

This material is available free of charge via the Internet at http://pubs.acs.org.

■ AUTHOR INFORMATION

Corresponding Author

*Fax: +1-617-258-5766. E-mail: braatz@mit.edu.

Notes

The authors declare no competing financial interest.

■ ACKNOWLEDGMENTS

The authors thank Mettler−Toledo International, Inc., for their loan of equipment, and Nilesh Shah, Mitsuko Fujiwara, Erja Kajosalo, Hong Jang, Herui Dou, Min Su, Ying Diao, Li Tan, and Anjani Jha for technical discussions.

■ REFERENCES

(1) Michaels, A. S.; Colville, A. R., Jr. The Effect of Surface Active Agents on Crystal Growth Rate and Crystal Habit. *J. Phys. Chem.* **1960**, *64* (1), 13−19.

(2) Sano, C.; Nagashima, N.; Kawakita, T.; Iitaka, Y. Effects of Additives on the Crystal Habit of Monosodium L-Glutamate Monohydrate. *J. Cryst. Growth* **1990**, *99* (1−4, Part 2), 1070−1075.

(3) Weissbuch, I.; Addadi, L.; Lahav, M.; Leiserowitz, L. Molecular Recognition at Crystal Interfaces. *Science* **1991**, *253* (5020), 637−645.

(4) Ma, D. L.; Braatz, R. D. Worst-Case Analysis of Finite-Time Control Policies. *IEEE Trans. Control Syst. Technol.* **2001**, *9* (5), 766−774.

(5) Lewiner, F.; Févotte, G.; Klein, J. P.; Puel, F. An Online Strategy to Increase the Average Crystal Size during Organic Batch Cooling Crystallization. *Ind. Eng. Chem. Res.* **2002**, *41* (5), 1321−1328.

(6) Takiyama, H.; Shindo, K.; Matsuoka, M. Effects of Undersaturation on Crystal Size Distribution in Cooling Type Batch Crystallization. *J. Chem. Eng. Jpn.* **2002**, *35* (11), 1072−1077.

(7) Yang, G.; Kubota, N.; Sha, Z.; Louhi-Kultanen, M.; Wang, J. Crystal Shape Control by Manipulating Supersaturation in Batch Cooling Crystallization. *Cryst. Growth Des.* **2006**, *6* (12), 2799−2803.

(8) Snyder, R. C.; Studener, S.; Doherty, M. F. Manipulation of Crystal Shape by Cycles of Growth and Dissolution. *AIChE J.* **2007**, *53* (6), 1510−1517.

(9) Wan, J.; Wang, X. Z.; Ma, C. Y. Particle Shape Manipulation and Optimization in Cooling Crystallization Involving Multiple Crystal Morphological Forms. *AIChE J.* **2009**, *55* (8), 2049−2061.

(10) Bajcinca, N.; de Oliveira, V.; Borchert, C.; Raisch, J.; Sundmacher, K. Optimal Control Solutions for Crystal Shape Manipulation. *Comput.-Aided Chem. Eng.* **2010**, *28* (C), 751−756.

(11) Nagy, Z. K.; Fujiwara, M.; Braatz, R. D. Monitoring and advanced control of crystallization processes. In *Handbook of Industrial Crystallization*, 3rd Edition; Myerson, A., Erdemir, D., Eds.; Cambridge University Press: Oxford, U.K., 2014 (in press).

(12) Lovette, M. A.; Muratore, M.; Doherty, M. F. Crystal Shape Modification through Cycles of Dissolution and Growth: Attainable Regions and Experimental Validation. *AIChE J.* **2012**, *58* (5), 1465−1474.

(13) Patience, D. B.; Rawlings, J. B. Particle-Shape Monitoring and Control in Crystallization Processes. *AIChE J.* **2001**, *47* (9), 2125−2130.

(14) Gunawan, R.; David, L.; Fujiwara, M.; Richard, D. B. Identification of Kinetic Parameters in Multidimensional Crystallization Processes. *Int. J. Mod. Phys. B* **2002**, *16* (1−2), 367−374.

(15) Lee, K.; Lee, J. H.; Fujiwara, M.; Ma, D. L.; Braatz, R. D. Run-to-Run Control of Multidimensional Crystal Size Distribution in a Batch Crystallizer. *Proc. Am. Control Conf.* **2002**, *2*, 1013−1018.

(16) Puel, F.; Févotte, G.; Klein, J. P. Simulation and Analysis of Industrial Crystallization Processes through Multidimensional Population Balance Equations. Part 1: A Resolution Algorithm Based on the Method of Classes. *Chem. Eng. Sci.* **2003**, *58* (16), 3715−3727.

(17) Briesen, H. Simulation of Crystal Size and Shape by Means of a Reduced Two-Dimensional Population Balance Model. *Chem. Eng. Sci.* **2006**, *61* (1), 104−112.

(18) Ma, C. Y.; Wang, X. Z.; Roberts, K. J. Multi-Dimensional Population Balance Modeling of the Growth of Rod-Like L-Glutamic Acid Crystals using Growth Rates Estimated from in-Process Imaging. *Adv. Powder Technol.* **2007**, *18* (6), 707−723.

(19) Ma, C. Y.; Wang, X. Z. Crystal Growth Rate Dispersion Modeling Using Morphological Population Balance. *AIChE J.* **2008**, *54* (9), 2321−2334.

(20) Ma, C. Y.; Wang, X. Z.; Roberts, K. J. Morphological Population Balance for Modeling Crystal Growth in Face Directions. *AIChE J.* **2008**, *54* (1), 209−222.

(21) Liu, J. J.; Ma, C. Y.; Hu, Y. D.; Wang, X. Z. Effect of Seed Loading and Cooling Rate on Crystal Size and Shape Distributions in Protein Crystallization-A Study using Morphological Population Balance Simulation. *Comput. Chem. Eng.* **2010**, *34* (12), 1945−1952.

(22) Liu, J. J.; Ma, C. Y.; Hu, Y. D.; Wang, X. Z. Modelling Protein Crystallisation using Morphological Population Balance Models. *Chem. Eng. Res. Des.* **2010**, *88* (4), 437−446.
(23) Calderon De Anda, J.; Wang, X. Z.; Lai, X.; Roberts, K. J. Classifying Organic Crystals Via in-Process Image Analysis and the use of Monitoring Charts to Follow Polymorphic and Morphological Changes. *J. Process Control* **2005**, *15* (7), 785−797.
(24) De Calderon Anda, J.; Wang, X. Z.; Roberts, K. J. Multi-Scale Segmentation Image Analysis for the in-Process Monitoring of Particle Shape with Batch Crystallisers. *Chem. Eng. Sci.* **2005**, *60* (4), 1053−1065.
(25) De Calderon Anda, J.; Wang, X. Z.; Lai, X.; Roberts, K. J.; Jennings, K. H.; Wilkinson, M. J.; Watson, D.; Roberts, D. Real-Time Product Morphology Monitoring in Crystallization Using Imaging Technique. *AIChE J.* **2005**, *51* (5), 1406−1414.
(26) Eggers, J.; Kempkes, M.; Mazzotti, M. Measurement of Size and Shape Distributions of Particles through Image Analysis. *Chem. Eng. Sci.* **2008**, *63* (22), 5513−5521.
(27) Larsen, P. A.; Rawlings, J. B.; Ferrier, N. J. An Algorithm for Analyzing Noisy, In Situ Images of High-Aspect-Ratio Crystals to Monitor Particle Size Distribution. *Chem. Eng. Sci.* **2006**, *61* (16), 5236−5248.
(28) Oullion, M.; Puel, F.; Févotte, G.; Righini, S.; Carvin, P. Industrial Batch Crystallization of a Plate-Like Organic Product. In Situ Monitoring and 2D-CSD Modelling: Part 1: Experimental Study. *Chem. Eng. Sci.* **2007**, *62* (3), 820−832.
(29) Pöllänen, K.; Häkkinen, A.; Reinikainen, S.-P.; Louhi-Kultanen, M.; Nyström, L. A Study on Batch Cooling Crystallization of Sulphathiazole: Process Monitoring using ATR-FTIR and Product Characterization by Automated Image Analysis. *Chem. Eng. Res. Des.* **2006**, *84* (1), 47−59.
(30) Puel, F.; Marchal, P.; Klein, J. Habit Transient Analysis in Industrial Crystallization using Two Dimensional Crystal Sizing Technique. *Chem. Eng. Res. Des.* **1997**, *75* (2), 193−205.
(31) Wang, X. Z.; Calderon De Anda, J.; Roberts, K. J. Real-Time Measurement of the Growth Rates of Individual Crystal Facets using Imaging and Image Analysis: A Feasibility Study on Needle-Shaped Crystals of L-Glutamic Acid. *Chem. Eng. Res. Des.* **2007**, *85* (7 A), 921−927.
(32) Wang, X. Z.; Roberts, K. J.; Ma, C. Crystal Growth Measurement using 2D and 3D Imaging and the Perspectives for Shape Control. *Chem. Eng. Sci.* **2008**, *63* (5), 1173−1184.
(33) Kempkes, M.; Eggers, J.; Mazzotti, M. Measurement of Particle Size and Shape by FBRM and In Situ Microscopy. *Chem. Eng. Sci.* **2008**, *63* (19), 4656−4675.
(34) Grön, H.; Mougin, P.; Thomas, A.; White, G.; Wilkinson, D.; Hammond, R. B.; Lai, X.; Roberts, K. J. Dynamic in-Process Examination of Particle Size and Crystallographic Form Under Defined Conditions of Reactant Supersaturation as Associated with the Batch Crystallization of Monosodium Glutamate from Aqueous Solution. *Ind. Eng. Chem. Res.* **2003**, *42* (20), 4888−4898.
(35) Togkalidou, T.; Tung, H.-H.; Sun, Y.; Andrews, A.; Braatz, R. D. Solution Concentration Prediction for Pharmaceutical Crystallization Processes using Robust Chemometrics and ATR FTIR Spectroscopy. *Org. Process Res. Dev.* **2002**, *6* (3), 317−322.
(36) Togkalidou, T.; Tung, H.-H.; Sun, Y.; Andrews, A. T.; Braatz, R. D. Parameter Estimation and Optimization of a Loosely Bound Aggregating Pharmaceutical Crystallization using in Situ Infrared and Laser Backscattering Measurements. *Ind. Eng. Chem. Res.* **2004**, *43* (19), 6168−6181.
(37) Ma, D. L.; Tafti, D. K.; Braatz, R. D. High-Resolution Simulation of Multidimensional Crystal Growth. *Ind. Eng. Chem. Res.* **2002**, *41* (25), 6217−6223.
(38) Ma, D. L.; Tafti, D. K.; Braatz, R. D. Optimal Control and Simulation of Multidimensional Crystallization Processes. *Comput. Chem. Eng.* **2002**, *26* (7−8), 1103−1116.
(39) Gunawan, R.; Fusman, I.; Braatz, R. D. High Resolution Algorithms for Multidimensional Population Balance Equations. *AIChE J.* **2004**, *50* (11), 2738−2749.
(40) Qamar, S.; Noor, S.; Ain, Q. U.; Seidel-Morgenstern, A. Bivariate Extension of the Quadrature Method of Moments for Batch Crystallization Models. *Ind. Eng. Chem. Res.* **2010**, *49* (22), 11633−11644.
(41) Sano, C.; Nagashima, N.; Kawakita, T.; Iitaka, Y. Crystal and Molecular Structures of Monosodium L-Glutamate Monohydrate. *Anal. Sci.* **1989**, *5* (1), 121−122.
(42) Togkalidou, T.; Fujiwara, M.; Patel, S.; Braatz, R. D. Solute Concentration Prediction using Chemometrics and ATR-FTIR Spectroscopy. *J. Cryst. Growth* **2001**, *231* (4), 534−543.
(43) Fujiwara, M.; Chow, P. S.; Ma, D. L.; Braatz, R. D. Paracetamol Crystallization Using Laser Backscattering and ATR−FTIR Spectroscopy: Metastability, Agglomeration, and Control. *Cryst. Growth Des.* **2002**, *2* (5), 363−370.
(44) Shoji, M.; Eto, T.; Takiyama, H. A Kinetic Study of the Influence of Modulated Undersaturation Operation on Crystal Size Distribution in Cooling-Type Batch Crystallization. *J. Chem. Eng. Jpn.* **2011**, *44* (3), 191−196.
(45) Rusli, E.; Lee, J. H.; Braatz, R. D. Optimal Distributional Control of Crystal Size and Shape. In *Proceedings of the Fifth World Congress on Particle Technology*, Orlando, FL, 2006; Paper No. 240f.
(46) Qamar, S.; Mukhtar, S.; Seidel-Morgenstern, A. Efficient Solution of a Batch Crystallization Model with Fines Dissolution. *J. Cryst. Growth* **2010**, *312* (20), 2936−2945.
(47) Nagy, Z. K.; Aamir, E.; Rielly, C. D. Internal Fines Removal using Population Balance Model Based Control of Crystal Size Distribution Under Dissolution, Growth and Nucleation Mechanisms. *Cryst. Growth Des.* **2011**, *11* (6), 2205−2219.
(48) Zhu, X.; Zhou, L.; Braatz, R. D. A Pure Method of Characteristics Approach for the Simulation of Particle Size Distribution in Complex Particulate Processes, 2013 (Technical report).
(49) Beck, J. V.; Arnold, K. J. *Parameter Estimation in Engineering and Science*; Wiley: New York, 1977.
(50) Rawlings, J. B.; Miller, S. M.; Witkowski, W. R. Model Identification and Control of Solution Crystallization Processes: A Review. *Ind. Eng. Chem. Res.* **1993**, *32* (7), 1275−1296.
(51) Randolph, A. D.; Larson, M. A. *Theory of Particulate Processes: Analysis and Techniques of Continuous Crystallization*, 2nd Edition; Academic Press: New York, 1974.
(52) Sherwood, J. N.; Ristic, R. I. The Influence of Mechanical Stress on the Growth and Dissolution of Crystals. *Chem. Eng. Sci.* **2001**, *56* (7), 2267−2280.
(53) Miller, S. M.; Rawlings, J. B. Model Identification and Control Strategies for Batch Cooling Crystallizers. *AIChE J.* **1994**, *40* (8), 1312−1327.
(54) Montgomery, D. C.; Runger, G. C. *Applied Statistics and Probability for Engineers*, 3rd Edition; Wiley: New York, 2002.